CRYSTAL GROWTH & DESIGN

pubs.acs.org/crystal

Article

Protein Crystallization in the Presence of a Metastable Liquid–Liquid Phase Separation

Published as part of a Crystal Growth and Design virtual special issue on Nonclassical Crystallization in Synthetic and Natural Systems.

Ralph Maier, Georg Zocher, Andrea Sauter, Stefano Da Vela, Olga Matsarskaia, Ralf Schweins, Michael Sztucki, Fajun Zhang,* Thilo Stehle,* and Frank Schreiber

Cite This: *Cryst. Growth Des.* 2020, 20, 7951–7962

Read Online

ACCESS | Metrics & More | Article Recommendations | Supporting Information

ABSTRACT: We study protein crystallization in solutions of human serum albumin (HSA) exhibiting a metastable liquid–liquid phase separation (LLPS) in the presence of trivalent salts. Specifically, we focus on the effects of dense liquid phases (DLPs) on the crystallization pathways. On the basis of the phase diagram, we choose two conditions around the LLPS binodal: one condition is located close to, but outside the LLPS region, resulting in protein clusters, but no macroscopic LLPS. Yet, a surface-enhanced unstable DLP layer is observed at the surface of the cuvette (wetting). The second condition, inside the LLPS binodal, leads to a macroscopic metastable DLP. The crystallization is followed by optical microscopy and small-angle X-ray and neutron scattering (SAXS/SANS) as well as by ultraviolet–visible spectroscopy to explore the role of LLPS. In no case evidence of nucleation inside the DLP is observed. SAXS and SANS show a monotonous growth of the crystals and a decrease of the overall material in the sample. We thus conclude that the existence of a metastable LLPS is not a sufficient condition for a two-step nucleation process. The DLP serves as a reservoir and crystal growth can be described by the Bergeron process, i.e., crystals grow directly into the dilute phase at the expense of the DLP. Furthermore, the crystallographic analysis of the resulting crystals shows that crystals with different morphology grown under different conditions share a similar crystal structure and that the metal ions create two bridging contacts within the unit cell and stabilize it.

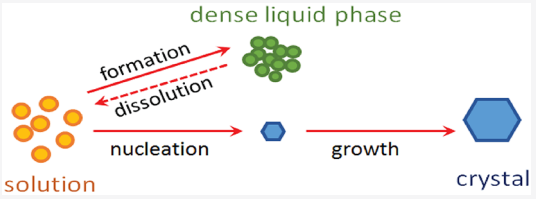

INTRODUCTION

Knowledge of protein structures is essential for the mechanistic understanding of their functions. Crystallography remains the most powerful tool in this context, but crystal structure determination of macromolecules is often hampered by a lack of high-quality crystals suitable for diffraction. One of the main challenges in the process of crystallization is the quantitative understanding and control of protein–protein interactions under various conditions and at different length scales and how these translate ultimately into crystallization. Since multiple parameters such as temperature, concentration of both protein and potential precipitants, the nature of the precipitants, solvent, etc. are involved in protein crystallization, predictions about the process are difficult to make.

For many years, classical nucleation theory (CNT) has been used to describe crystallization.[1−3] It states that a nucleus forms directly from a supersaturated solution. Nevertheless, recent theoretical, experimental, and simulation studies have revealed nonclassical features in the early stage of nucleation for several systems.[4−11] In particular, the decoupling of the order parameters involved during a fluid-to-solid transition leads to the so-called two-step nucleation mechanism, in which a metastable intermediate phase (MIP) exists between the initial supersaturated solution and the final crystals. Depending on the exact free energy landscapes, the MIPs can be a high density liquid phase, mesoscopic clusters, or a preordered state.[12−15]

For colloid and protein systems, dominating short-ranged attractive interactions lead to a metastable liquid–liquid phase separation (LLPS) with respect to the fluid-to-solid transition.[16] As illustrated in Figure 1a, the LLPS coexistence line is located below the solubility line, indicating the metastability with respect to the crystalline phase. LLPS may be interrupted by glass formation of the dense phase and result in an arrested state.[17]

In terms of protein crystallization, the existence of a metastable LLPS region may be the main reason underlying the formation of MIPs, as indicated by three possible pathways of two-step nucleation associated with LLPS (paths 1–3)

Received: September 1, 2020
Revised: October 29, 2020
Published: November 18, 2020

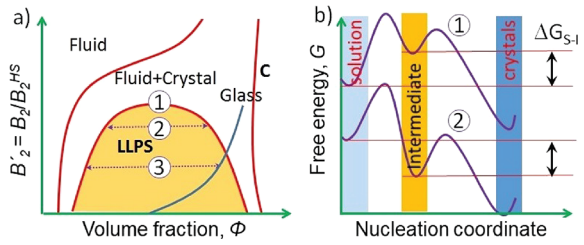

Figure 1. (a) Typical phase diagram for colloidal systems with short-range attractions including protein solutions. Three possible nucleation paths associated with LLPS are indicated (see text for details). (b) Free energy landscapes for the nucleation paths 1 and 2 labeled in (a).

which can be identified in Figure 1. The exact pathways depend on the respective quench depths and their resulting locations in the phase diagram.[5] The starting point for the respective paths is always the single-phase region with higher reduced second virial coefficients, $B_2' = B_2/B_2^{HS}$, thus, a stable fluid solution. B_2' is a measure of the interaction strength between two proteins and B_2^{HS} is the second virial coefficient of hard spheres with a radius R. Lower negative B_2'-values indicate an increased attraction between the proteins. B_2' can be tuned by, for example, varying the temperature or the solvent.[18−23] Path 1 (quench down to 1 in Figure 1a, representing the region near the critical point of LLPS where density fluctuations occur) leads to a two-step nucleation as initially proposed by ten Wolde and Frenkel.[12] Path 2, quenching down to 2 in Figure 1a, representing conditions inside the LLPS binodal, suggests that LLPS occurs before nucleation and that both dilute and dense phase are liquid-like. The two-step theory predicts crystal nucleation inside the macroscopically dense liquid.[8,12,13] Path 3, i.e., a quench down to 3, suggests that for a deeper quench the binodal of the high density branch is intercepted by the "glass line", resulting in an arrested nonequilibrium state of the dense phase.[17,18] In this case, nucleation within the dense phase is hindered by dynamical arrest.[17] Compared to the CNT, the respective free energy landscapes of these nonclassical pathways thus show an additional free energy minimum (Figure 1b), corresponding to the intermediate phase. If the free energy of the intermediate phase is higher than that of the initial solution (top curve in Figure 1b), it is unstable with respect to the initial solution (but still in a local free energy minimum) and the MIP exists as mesoscopic clusters. If the free energy of the intermediate phase is lower than that of the initial solution (bottom curve in Figure 1b), then the MIP can be a metastable dense liquid phase (DLP).[24] In both cases, the MIPs have a higher free energy than the crystals and thus are not stable with respect to crystallization.

In our previous work, we have demonstrated that multivalent salts can be used to induce a phase behavior similar to that described in Figure 1a as well as crystallization of globular proteins.[25−29] Transition metals, including especially lanthanides and yttrium, have recently become more and more popular since they are used for the structure determination of hundreds of proteins by X-ray diffraction and nuclear magnetic resonance (NMR) and are found in lanthanide-dependent metalloenzymes in bacteria.[30−32] One example is their presence in the active site of methanol dehydrogenase, which is involved in the metabolism of multicarbon substrates.[31,33] We have shown that negatively charged globular proteins at a neutral pH undergo a reentrant condensation (RC) phase behavior in the presence of trivalent salts. RC has been originally observed for DNA[34] and has also been described in systems of globular proteins in the presence of multivalent ions.[5,28,29,35−39] Since HSA is initially net negatively charged at neutral pH,[36] the proteins repel each other at a given protein concentration and form a clear and stable solution (regime I, see also Figure 2 further below). By increasing the salt

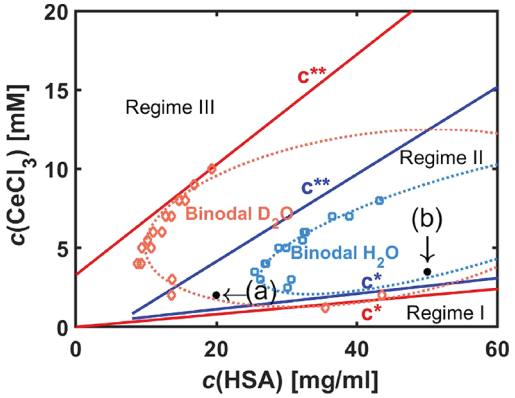

Figure 2. Experimental phase diagram of HSA with $CeCl_3$ in H_2O (blue) and in D_2O (red) at room temperature. Both RC and LLPS exist in both solvents, but replacing H_2O by in D_2O significantly broadens the phase boundaries due to an enhanced interprotein attraction.[23] The crystallization conditions examined in this paper are labeled as (a) outside the LLPS area in H_2O and (b) inside the LLPS area for both solvents. The dotted binodal ellipses are guides to the eye. The solid lines represent fits for c^* and c^{**} in the respective system, determined by visual inspection.

concentration (c_s) above a well-defined salt concentration (c^*), the proteins aggregate or condense due to binding the multivalent ions, diminishing the negative charge of the proteins (regime II). The solution thereby turns turbid. Increasing c_s even further, above the second well-defined salt concentration c^{**}, leads to an effective charge inversion of the proteins.[28,39] Thereby, the attraction between the proteins becomes weaker and a stable and clear solution is observed again (regime III). This charge inversion of proteins can also be obtained *vice versa*, i.e., by adding negatively charged polyoxometalates (POMs) to positively charged proteins in sufficient concentrations.[40] For details, see refs 41, 36, and 29.

Having illustrated the phase behavior of aqueous solutions of globular proteins in the presence of multivalent salts, we proceed to explain its implications for crystallization. In our system, a metastable LLPS region exists inside regime II (see Figure 2).[29,37,39,42] According to the literature, crystallization from the condensed regime may follow different pathways. Near c^*, crystals grow directly from the supersaturated solutions; near or inside the LLPS binodal, metastable LLPS occurs first and is followed by crystal growth.[5,25−29,37,43,44]

An important theoretical prediction of the two-step theory is that nucleation is favored inside the dense liquid intermediate phase compared to the dilute phase, since the surface energy of the dense phase is closer to the final crystalline state, and thus the free energy barrier for nucleation is lower.[8,12,13] However, experimental observations in several protein systems suggest that crystals nucleate mainly from the dilute phase or at the interface of the dense liquid droplets and grow outside of it into the dilute phase.[45−47] These observations are often

https://dx.doi.org/10.1021/acs.cgd.0c01219
Cryst. Growth Des. 2020, 20, 7951−7962

ascribed to the high viscosity or even gel-like state of the DLP.[17]

In spite of significant progress, many questions are still open regarding the role of this metastable LLPS for nucleation and the subsequent crystal growth. In this paper, we use the protein HSA with yttrium chloride (YCl_3) and cerium chloride ($CeCl_3$) as a model system to study the effect of metastable LLPS on crystallization. For HSA with $CeCl_3$, we use both H_2O and D_2O as solvents since one can tune protein−protein interactions by exchanging hydrogen with deuterium.[20−23] In particular, we focus on whether crystals can nucleate and grow inside the DLP after LLPS. For this purpose, conditions inside and near the LLPS binodal, corresponding to metastable and unstable LLPS, respectively, are chosen for the crystallization study. We note that, in the present article, the term "unstable LLPS" implies that the LLPS is unstable with respect to both the initial solution and the crystalline phase. In contrast, metastable dense phases are more stable than the initial solution, but have a higher free energy than crystals (see Figure 1b).

The results presented here provide insights into the role of LLPS in crystallization processes. Importantly, in addition to the kinetic insights, we further report a new crystal structure of HSA with metal ions incorporated in the crystal lattice, highlighting the crucial role of the multivalent ions in the crystallization process by forming intermolecular contacts.

EXPERIMENTS AND METHODS

Materials and Sample Preparation. Protein, salts and D_2O were purchased from Sigma-Aldrich, now Merck, and used as received. The guaranteed purities were 97% for HSA (A9511), 99.99% for $CeCl_3$ (429406) and YCl_3 (451363), and 99.9% for D_2O (151882).

All samples were prepared by mixing the required amount of salt stock solution, deionized (18.2 MΩ) degassed Millipore water or D_2O (for neutron scattering experiments) and protein stock solution. Stock solutions were prepared by dissolving the protein and salt powders in deionized degassed Millipore water or D_2O, respectively. The concentration of HSA solutions was determined by UV absorption measurements using an extinction coefficient of 0.531 $L{\cdot}g^{-1}{\cdot}cm^{-1}$ at a wavelength of 278 nm.[48] A Seven Easy pH instrument from Mettler Toledo was used to monitor the pH of the protein solutions. All samples had a pH (between 6.2 and 6.9) above the pI of HSA. No additional buffer was used to avoid the effect of co-ions.

METHODS

Optical Microscopy. An optical microscope (Axio Scope.A1, Carl Zeiss AG) was used for optical investigations of the samples. Images were recorded by a camera (AxioCam ICc5, Carl Zeiss AG) in combination with the software ZEN Lite 2012. The samples were prepared in two different ways. In the first case, ∼50 μL of solution were pipetted into a silicone ring on a glass slide, and covered with a cover slide. Alternatively, ∼350 μL were filled into a type 120 quartz glass cuvette (Hellma GmbH, Müllheim, Germany) with a path length of 1 mm. After mixing the samples in a separate tube, they were filled into the quartz cuvettes, which were subsequently sealed with Parafilm.

UV−Visible Spectroscopy (UV−vis). UV−vis was used to follow the change in protein concentration of the dilute phase during crystal growth in the presence of a metastable DLP. The experiments were performed with a UV−vis spectrophotometer (Cary 50 UV−vis spectrometer, Varian Technologies, USA). The solutions were probed in a quartz cuvette with a path length of 1 mm. UV−vis spectra were collected every 10 min over a period of several days.

Determination of the Phase Diagram. The phase diagram of Figure 2 was determined following the procedure established in our group as reported in previous work.[37,42] The respective c^* and c^{**} phase transition boundaries (with $c^{**} < c^*$) were determined by visual inspection of 200 μL samples at c_p = 10, 15, 20, 22.5, 25, 30 35, 40, and 50 mg/mL HSA in H_2O and c_p = 10, 20, 35, and 50 mg/mL HSA in D_2O and varying c_s. The mean of the c_s of the last clear and first turbid or last turbid and first clear sample is referred to as c^* or c^{**}, respectively. The LLPS binodals in the phase diagram (Figure 2) were determined using UV−vis spectroscopy. Samples were prepared at 35 and 45 mg/mL HSA and varying c_s for both solvents H_2O and D_2O. The macroscopically liquid−liquid phase-separated state of these samples was verified by visual inspection. The sample tubes were centrifuged for 2 min with 21030 x g to separate the dilute and the dense phases. The concentration of the dilute phase was determined by the UV−vis spectrophotometer.

Small Angle X-ray Scattering (SAXS). SAXS measurements were performed at the European Synchrotron Radiation Facility (ESRF), Grenoble, France, at beamline ID02.[49] The sample-to-detector distance was set to 2 m. The energy of the incoming X-rays was 12 keV, covering a q-range from 0.25 to 3.2 nm^{-1}. The exposure time was 0.1 s for each measurement. The crystals were collected and filled into a quartz capillary with a wall thickness of about 10 μm and a diameter of 2 mm. The sample capillary was inserted into the beam vertically. During the measurement, the capillary was shifted up and down to measure the scattering pattern at different positions. The 2D intensity pattern was calibrated to absolute intensity and azimuthally averaged to obtain the intensity profiles. The averaged profiles from different positions were used to index the Bragg peaks. More detailed information on data reduction and q-resolution calibration can be found in the literature.[50,51]

Additional SAXS data were collected on a laboratory instrument (Xeuss 2.0, Xenocs, Grenoble, France) employing a GeniX 3D microfocus X-ray tube with a copper anode, using an X-ray wavelength of 1.54 Å. With a sample-to-detector distance of 1850 mm, the employed Pilatus 300 K detector covered a q-range from 0.055 to 2.25 nm^{-1}. Quartz capillaries with a diameter of 2 mm were used. The acquisition time per run was 10 min.

Small Angle Neutron Scattering (SANS). SANS measurements were carried out at beamline D11 at the Institut Laue-Langevin (ILL), Grenoble, France.[52] The sample-to-detector distance was 2 m, which covers a q-range from 0.03 to 0.33 $Å^{-1}$ at a wavelength of 6 Å ($\Delta\lambda/\lambda$ = 10%). Protein-salt solutions in D_2O were filled into rectangular quartz cells with a path length of 2 mm. The beam size on the sample was 7 mm × 10 mm. The acquisition time per run was 240 s. Runs were repeated in appropriate time intervals in order to follow the crystallization process over a period up to several days. H_2O was used as secondary calibration standard to calibrate the absolute scattering intensity. Data were stored in the NeXus data format.[53] The data correction and absolute intensity calibration were performed using the software LAMP.[54] Data can be accessed via the DOI given in ref 55.

Protein Crystallization and Crystal Structure Analysis. High-quality protein single crystals were obtained for a sample containing 31.0 mg/mL HSA and 2 mM YCl_3 at 293 K by batch crystallization in small glass vials.

Single crystals were pipetted onto a siliconized glass plate and subsequently subjected to a stepwise cryo-protection using the mother liquor, i.e., H_2O with the respective c_s, supplemented with 26% (v/v) glycerol. Crystals were mounted into a loop prior to flash-freezing in liquid nitrogen. Data were recorded at beamline X06SA at the Swiss Light Source (SLS), Villigen, Switzerland. A highly redundant data set was recorded at a wavelength of 1.7 Å to maximize the anomalous signal of the yttrium ions (Table S1). The data were reduced using the XDS package.[56] Phases were obtained by the molecular replacement procedure of PHASER[57] using HSA as template structure (PDB code: 2BXI) followed by a simulated annealing approach as implemented in PHENIX[58] to reduce the model bias. The following refinement was done in several cycles of reciprocal space refinement as implemented in REFMAC5[59] followed by real space model corrections using COOT.[60] Positions of the metal ions were determined on the basis of a $|F^+-F^-|$-electron density map. The structure was validated using MOLPROBITY,[61] visualized with

https://dx.doi.org/10.1021/acs.cgd.0c01219
Cryst. Growth Des. 2020, 20, 7951−7962

PYMOL,[62] and deposited to the Protein Data Bank with accession code 7A9C.

RESULTS AND DISCUSSION

Experimental Phase Diagram of the HSA−$CeCl_3$ System at Room Temperature. First, we present the phase diagram and the crystallization conditions of our systems. Figure 2 summarizes the phase behavior including reentrant condensation and LLPS of HSA−$CeCl_3$ in H_2O and in D_2O. For this system, the second regime and the LLPS region in D_2O are significantly broadened in comparison to H_2O. In essence, the c^{**} boundary is shifted to higher salt concentrations, whereas c^* remains approximately at the same location. The LLPS binodal is also shifted to much lower protein concentrations in D_2O. The shift of the phase boundaries results from enhanced attractive interactions in D_2O as reported in our previous work on a similar system.[23] This solvent isotope effect has been observed for several other proteins, such as lysozyme and γB-crystallin solutions.[20−22] In contrast to its bovine variant bovine serum albumin (BSA), which we have also investigated in detail (see refs 19, 23, 35, 36, 41, and 63−65) and which also shows RC, LLPS and a tunable phase behavior using a deuterated vs protonated solvent,[23] crystallization of HSA is readily observed in the presence of multivalent salts. We have investigated HSA with YCl_3 before as well,[42] but the HSA−$CeCl_3$ system crystallizes in a more controlled fashion and is therefore used as a model system. Another advantage for the purpose of this work is the clearly visible LLPSregion, which is mostly not the case for β-lactoglobulin systems.

The experimental phase diagram provides a guide for optimal conditions of protein crystallization. Slightly below c^*, macroscopic needle-like crystals are formed and no visible intermediate phase is observed. Crystals appear directly in the clear supersaturated solution.[25,26] For HSA with $CeCl_3$, the crystals feature predominantly lenticular shapes (see Figure 3 and Figure 5). Different morphologies of crystals grown in the presence of YCl_3 are shown in Figure S1. We found that near c^* and at the lower boundary of the LLPS binodal, proteins crystallize reproducibly.[37] In the present work, we choose two typical conditions around the LLPS binodal as labeled in Figure 2. The first condition (a) is located outside of the binodal. Under this condition, protein clusters exist, but macroscopic LLPS is impossible. However, at the liquid/solid interface, a surface-enhanced wetting layer of dense phase may form, meaning that the DLP can only exist at a surface stabilizing it due to its location outside the binodal in the phase diagram.[66] Thus, the free energy of the dense phase is even higher than that of the initial supersaturated solution and corresponds to path 1 shown in Figure 1. The second condition (corresponding to position b in Figure 2) is located inside the LLPS region, where macroscopic LLPS leads to a protein-rich and a protein-poor phase. Both are metastable with respect to the crystalline phase. This condition corresponds to path 2 in Figure 1. These crystallization areas at constant temperatures in the phase diagram are consistent with theoretical predictions.[37,67]

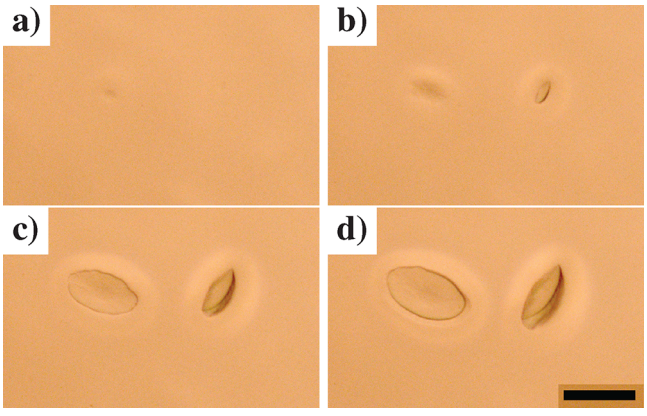

Figure 3. Bright field optical microscopy observations of crystallization of a sample containing 20 mg/mL HSA and 2.5 mM $CeCl_3$ at different times after preparation. The sample was briefly centrifuged in the cuvette before examination under the microscope in order to concentrate the protein aggregates on one site. Key: (a) 4.3 h, a small crystal appears at the wetting layer; (b) 5.7 h, a second crystal appears; (c) 7 h and (d) 7.7 h, crystal growth and consumption of the DLP lead to the formation of a depletion zone around the crystals. The scale bar corresponds to 50 μm.

Crystal Growth with Unstable LLPS: Path 1. We will first discuss the crystallization experiments for the samples located at position a in Figure 2. Figure 3 shows the crystallization process of a sample which is located outside the lower part of the LLPS region (20 mg/mL HSA and 2.5 mM $CeCl_3$ in H_2O). A depletion zone appears around the crystals. The formation of a depletion zone for a different salt concentration is shown in Figure S2, indicating reproducibility. Furthermore, an optical microscopy video of the sample in Figure 3 is shown in the Supporting Information, Movie S1, detailing the process of crystallization. In the phase diagram (Figure 2), condition a is located outside the LLPS binodal for H_2O. Nevertheless, it is visible that the unstable microscopic dense droplets sediment to the bottom, where they are able to form a layer on the glass surface. Since the dense droplets are visible only for several minutes by microscopy (in contrast to path 2), we expect them to be unstable with respect to the initial solution (see Figure 1b) and to completely dissolve again without an interface to sediment onto. Hence, this layer of dense phase is presumed to be a surface-enhanced phenomenon.[66]

Crystal growth kinetics for the same conditions was further studied using real-time SAXS and SANS. Real-time SAXS data of a sample containing 20 mg/mL HSA and 2 mM $CeCl_3$ are shown in Figure 4a. The SAXS profiles are initially smooth and the scattering intensity mainly stems from the protein form factor in the high q (>0.1 $Å^{-1}$) region. In the intermediate q-range, the overall attraction leads to an intensity increase with decreasing q. The low q (<0.01 $Å^{-1}$) upturn indicates the formation of protein clusters. No additional structural features from the protein clusters were seen, which is in contrast to the β-lactoglobulin (BLG)-$CdCl_2$ system we studied previously, where an additional protein−protein correlation peak reflects the presence of an intermediate phase.[26,27] Over time, the overall intensity decreases in the q-range measured, and after 10 h, the first Bragg peak appears at q = 0.069 $Å^{-1}$. For a quantitative analysis of the growth kinetics, we have integrated the intensities in the range from 0.03 to 0.06 $Å^{-1}$ and plotted the resulting values as a function of time in Figure 4b to follow the process of protein consumption from solution. This range was chosen for several reasons. First, since no additional structural feature is visible in the raw data indicating scattering from a different phase, one cannot distinguish contributions in the scattering signal from the wetting layer observed under the

https://dx.doi.org/10.1021/acs.cgd.0c01219
Cryst. Growth Des. 2020, 20, 7951−7962

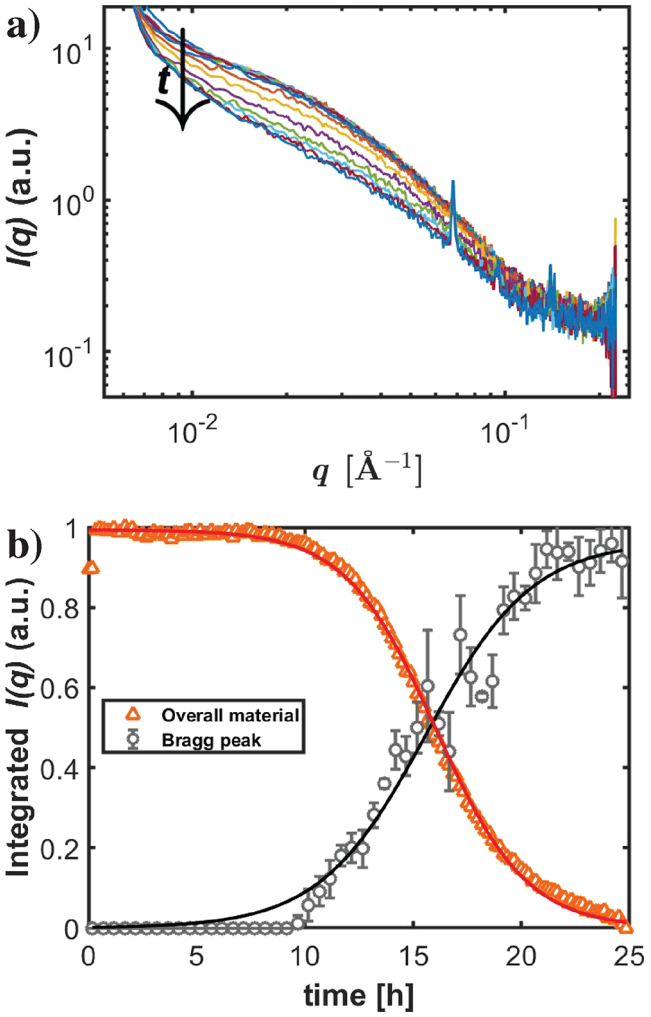

Figure 4. SAXS data of a sample containing 20 mg/mL HSA and 2 mM $CeCl_3$. (a) Scattering intensity curves between 0 and 25 h after sample preparation as functions of q and (b) analysis of the kinetics based on the integrated area covered by Bragg peaks and the low q-intensity between 0.03 and 0.06 Å^{-1}. The solid lines represent the corresponding fits (eq 1).

microscope and the dilute phase. Importantly, the structure factor dominates the signal in this q-region. The decrease in intensity is therefore attributed to the overall material consumption during crystallization. Second, it is accessible with both SAXS and SANS, and therefore, the data can be easily compared. Third, it does not overlap with the Bragg peaks, so these different contributions can be well separated. We have also integrated the q-range between the first and the second Bragg peak for all samples, leading to the same results. Last but not least, the statistical data quality is higher for lower q-values. The values for the area of the Gaussian fit of the Bragg peak at q = 0.069 Å^{-1} after subtracting a linear background are also plotted in order to follow crystal growth. One can see that the scattering intensity from the solution begins to decrease after ∼8 h. At the same time, the Bragg peak starts to grow. Both changes proceed monotonously and no stepwise change is visible. After ∼20 h, the Bragg peak intensity reaches a maximum value which remains nearly constant. In Figure 4b, data points of the Bragg peak fit were binned in groups of three to improve the statistics. The error bars represent the respective standard deviation. This procedure was not necessary for the SANS data, because the R^2-values of the Gaussian fits are all higher than 0.92. The error of the integrated scattering intensity of the overall material is always much smaller than the symbols, and thus not plotted for clarity. For all data sets (SAXS and SANS), both the intensity of the Bragg peak and of the proteins inside dense and dilute phase were fitted by a logistic function (eq 1), where A is the maximum of the curve, k its logistic growth rate or steepness, and t_1 the time of its midpoint.[68]

$$f(t) = \frac{A}{1 + e^{-k(t-t_1)}} \quad (1)$$

According to Arrhenius' law, the initial exponential increase in the intensity of the Bragg peak is caused by nucleation,[69] which is the rate-limiting step at this time. Later, the growth of the crystals is linear until it eventually reaches a plateau due to limited material in solution. Depending on how far away the solubility line is located from the LLPS binodal, crystals can still grow after all dense phase is consumed, since the dilute phase is then consumed (see also later). The midpoints for both curves in Figure 4b are $t_{1,Bragg}$ = 15.59 h and $t_{1,solution}$ = 16.04 h. The time of the midpoint, t_1, is also the time of the turning point of the curves and can be seen to be equal to the respective time of the extremum of the first time derivatives. Since the t_1-values are similar, indicating that proteins are consumed the fastest when crystals grow the fastest, this result suggests again a one-step process. All fit parameters are listed in Table S2.

A similar condition (inside the second regime, but outside the LLPS binodal) for the system in D_2O (10 mg/mL HSA with 2 mM $CeCl_3$ in D_2O) was studied by SANS. The results are shown in Figure S3. Both SAXS and SANS measurements show a similar growth behavior: first, around the Bragg peaks, no additional structural feature is visible, which could be used to identify the intermediate phase. Due to the crystal size, the crystals sediment to the bottom of the container once they are big enough. SANS has the advantage of a large scattering volume with a large number of crystals contributing to the scattered intensity. The results shown above indicate that given the current conditions, crystal growth can be described by a one-step crystallization. Combining this result with results from microscopy and UV−vis, we conclude that after nucleation in the dilute phase or at its interface with the dense phase or the container, the crystals grow into the dilute phase while they first consume the dense phase/wetting layer, followed by the dilute phase.

Crystal Growth with a Metastable LLPS: Path 2. We now present the results of crystal growth at position b in Figure 2, i.e., inside the LLPS binodal. We prepared one set of samples containing 50 mg/mL HSA and 3.5 mM $CeCl_3$, located at the lower binodal boundary of LLPS in the phase diagram. In this case, the amount of dense phase is small and it appears rather liquid-like than gel-like.

The crystal growth of this sample followed by optical microscopy is shown in Figure 5. Tiny droplets of DLP are visible right after preparation. Some of them sediment to the bottom surface while some stay in solution. The latter merge and disappear with time. In contrast to path 1 described previously, the droplets appear stable with respect to the initial solution (see Figure 1b), evidenced by their increased lifetimes. Crystals appear ∼2 h after preparation. While nucleation is not observed in the dense phase, it is seen in the dilute phase or at its interface with the container, which

https://dx.doi.org/10.1021/acs.cgd.0c01219
Cryst. Growth Des. 2020, 20, 7951−7962

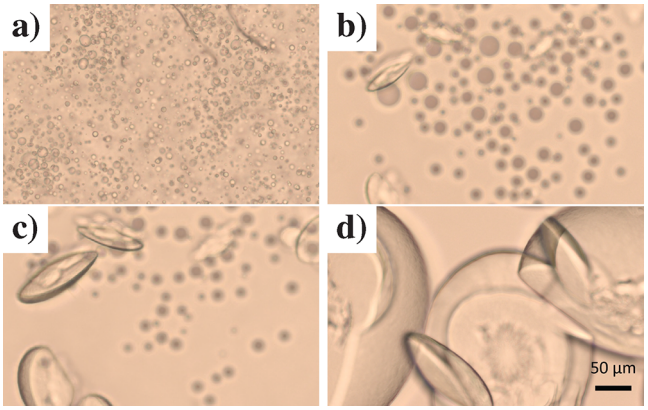

Figure 5. Crystal growth of a sample containing 50 mg/mL HSA and 3.5 mM $CeCl_3$ at different times after sample preparation: (a) 10 min; (b) 6 h; (c) 8 h; (d) 17 h. The scale bar corresponds to 50 μm.

suggests a one-step crystallization. The latter two scenarios cannot be distinguished due to the limited resolution of the optical microscope. After 17 h, the system is crystallized and no further changes can be observed on a reasonable time scale. Crystal growth first consumes the material (dense phase) around the crystals, leading to a depletion or "buffer zone". Similar observations have been reported for crystal growth in lysozyme solutions undergoing LLPS.[47] An interesting observation concerns the consumption of the dense phase upon crystal growth. Under the microscope, one can see that the droplets are shrinking, but neither do crystals grow into the droplets nor do droplets incorporate into the crystals. This suggests crystal growth via the deposition of proteins from the dilute phase. While the dilute phase feeds crystal growth, the droplets dissolve, i.e. the crystal growth does not consume the droplets directly.

In Figure 6, size measurements for three different crystals of the sample containing 50 mg/mL HSA and 3.5 mM $CeCl_3$ are

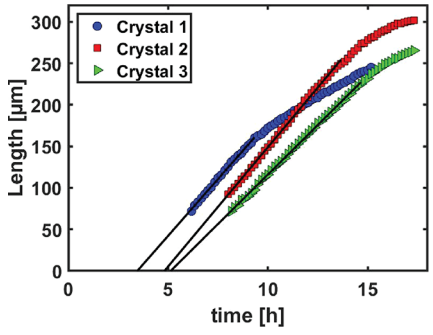

Figure 6. Crystal length as a function of time for the sample shown in Figure 5. After 11.7 h, no dense droplets can be observed anymore.

shown. In every case, the initial crystal growth follows a linear relationship. The fits are further extrapolated to obtain the induction times t_0 = 3.5, 4.8, and 5.1 h for crystals 1−3, respectively. Note that these measurements are performed for crystals in the focal area, which are not necessarily the ones that grew first. In addition to the growth rates and the induction times, the final sizes of the crystals (250 to 300 μm) are similar. The disappearance of the dense droplets seems to have no direct impact on their growth rate. The late stage saturation of the size can be explained by the limited amount of material in the solution. This linear growth behavior would be consistent with a one-step nucleation process.

The crystal growth kinetics was further characterized using SANS. Figure 7 shows SANS data and the corresponding

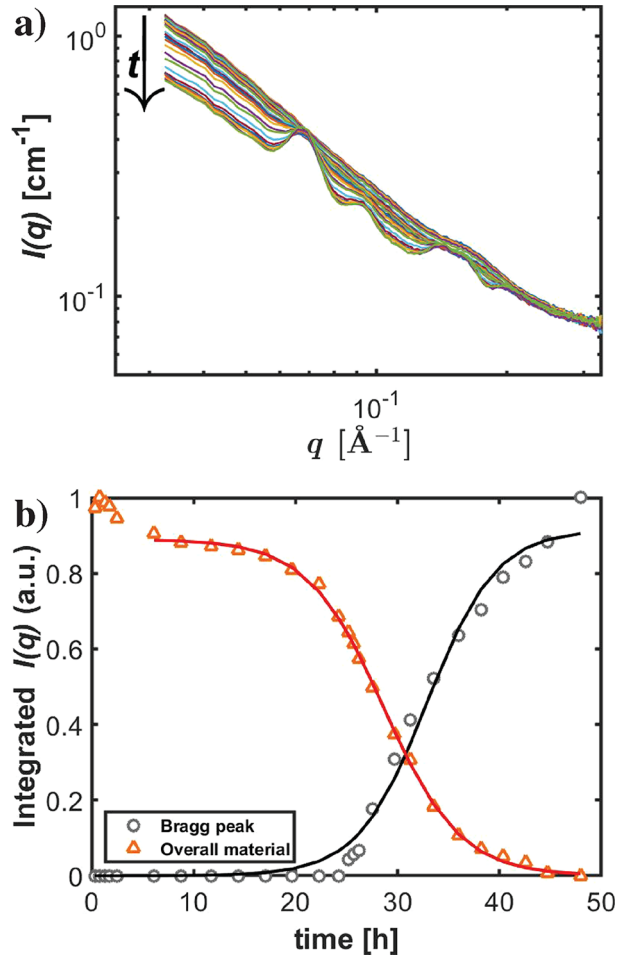

Figure 7. (a) SANS profiles of crystal growth of a sample containing 50 mg/mL HSA and 3.5 mM $CeCl_3$ in D_2O between 0 and 48 h. (b) Analysis of the kinetics based on the areas of the Bragg peak at q = 0.07 Å^{-1} and the normalized integral of intensity in the q-range from 0.03 to 0.06 Å^{-1} for the crystalline phase and the overall material, respectively. The solid lines represent the corresponding fits (eq 1).

analysis of a sample containing 50 mg/mL HSA with 3.5 mM $CeCl_3$ in D_2O. The corresponding optical microscopy images of the crystal growth in D_2O are presented in Figure S4. Although the appearance of the DLP is different in D_2O (network) than in H_2O (droplets) because of enhanced interprotein attractions in D_2O, crystal growth in H_2O and D_2O is comparable. Again, the overall smooth SANS curves show a decrease in intensity in the low q-region as shown in Figure 7a. With time, Bragg peaks appear and their areas increase. In addition to the overall material consumption, the area of the Gaussian fit of the first Bragg peak at q = 0.07 Å^{-1}, representing the crystalline phase, is plotted in Figure 7b. It increases with time, indicating crystal growth. Similar to Figure 4b, both changes are monotonous and no stepwise change is visible.

The slight decrease in intensity in the beginning may be due to the temperature difference between sample preparation and the measurement. Therefore, these data points were not taken

https://dx.doi.org/10.1021/acs.cgd.0c01219
Cryst. Growth Des. 2020, 20, 7951−7962

into account for the fit. Afterward, an initially exponential increase followed by a linear part of the Bragg peak area is visible again. The increase at later stages is more pronounced compared to the samples discussed before. The solubility line may be located further away from the LLPS binodal or some crystals may have sedimented from the top of the cuvette into the beam region, causing this increase. However, the respective t_1-values are similar again. This result is also consistent with a one-step crystallization where the metastable dense phase serves as a reservoir for the crystal growth and is consumed during the process. We would expect a stepwise growth for a two-step nucleation as can be, for example, observed for BLG with $CdCl_2$.[26,27]

To further clarify the role of the DLP in crystallization, we have determined the protein concentration of the dilute phase during crystal growth. After preparation, the samples were briefly centrifuged in order to deposit the dense phase at the bottom of the cuvette. The protein concentration of the dilute phase was followed by UV−vis as shown in Figure 8a. The

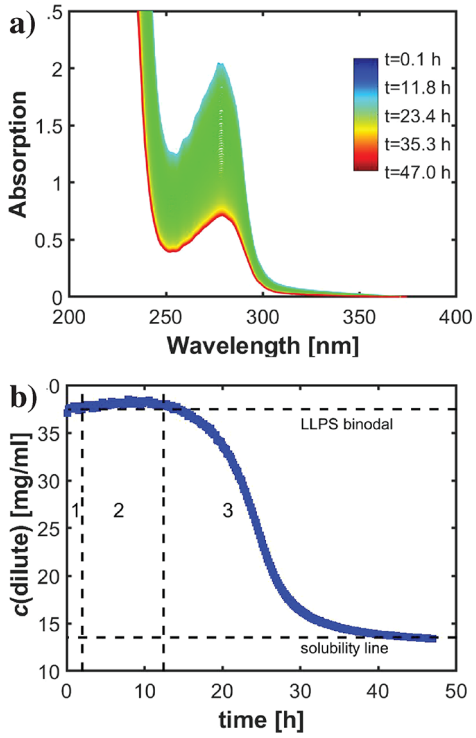

Figure 8. Protein concentration of the dilute phase during crystal growth of a sample containing 50 mg/mL HSA and 3.5 mM $CeCl_3$ monitored by UV−vis spectroscopy. (a) Real-time UV−vis spectra and (b) protein concentration as a function of time. On the basis of microscopy data (exemplarily shown in Figure 5), we distinguish three sections. In section 1, no crystals are formed yet, while they nucleate and consume the dense droplets in section 2 and grow further without a visible dense phase in section 3.

protein concentration in the dilute phase as a function of time is plotted in Figure 8b and can be divided into three stages: first (from the beginning to about 15 h) the protein concentration is almost constant and corresponds to the dilute phase resulting from LLPS. During this time, crystals are already formed, but crystal growth consumes the dense phase, and thus, the dilute phase has an almost constant concentration. The minor increase in protein concentration can be caused by a slight temperature difference between the centrifuge and the UV−vis spectrophotometer. In the second stage, the concentration decreases quickly with time, corresponding to a growth process of the crystals while consuming the dilute phase. In the third stage, the protein concentration of the dilute phase is low, corresponding to the gas−solid (solution-crystal) equilibrium, i.e., the solubility line.

Discussion of the Role of Metastable LLPS for Protein Crystallization. In summary, our growth kinetics studies by optical microscopy for individual crystals as well as by real-time SANS/SAXS and UV−vis for the overall growth kinetics lead to the consistent conclusion that the crystal nucleation for the present system follows a one-step process and the intermediates (dense liquid droplets/wetting layer or protein clusters) serve as a reservoir. Such a growth pathway is illustrated in Figure 9.

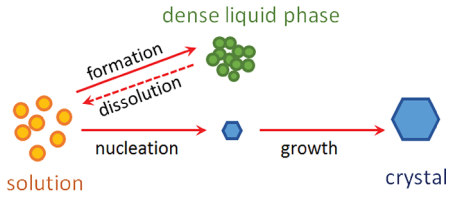

Figure 9. Schematic of the nucleation pathway of protein crystallization in the presence of a metastable LLPS as revealed from this study.

Two-step nucleation theory predicts that a metastable high density liquid phase is favored for crystal nucleation because of the lower free energy barrier. However, any experimental studies indicate that crystals form either inside the dilute phase or at the interface between the dense and dilute phase and grow into the dilute phase. This has been attributed to the arrested state of the dense phase.[45−47] This may indeed be the case for lysozyme.[17] The fact that the dense phases studied in the present work are always able to merge as well as dissolve again, similar to the study by Ray and Bracker,[46] indicates, however, that they are liquid-like. Thus, the slow dynamics cannot be used to explain the absence of nucleation inside the dense phase. We expect that a combination of heterogeneous and homogeneous nucleation may be the alternative. Due to the low resolution limit of the optical microscope, one cannot unambiguously determine if nucleation takes place at impurities, at interfaces of the dilute phase with the dense phase or with the sample container, or directly in the dilute phase. Nevertheless, nucleation inside the dense phases was not visible in any of our experimental conditions, even with extremely long lifetimes of the metastable ones. We speculate that to some extent the mechanism of enhanced adsorption (and possibly crystal nucleation) at the interface of the glass container may play a role, but a detailed study of this is beyond the scope of the present work and can be found in refs 64 and 65.

We note that observations of two-step processes involving manifold kinds of precursors have been made for several proteins.[4,5,13,15,25−27,70-73] We do not completely rule out the possibility that different precursors with a short lifetime in solution may initiate crystal nucleation (which is beyond the resolution limitation of the microscope and which we also do not observe with SAXS/SANS). In our work, we aim to investigate the role of macroscopic LLPS on nucleation. The macroscopic dense droplets are clearly visible under the microscope, and their lifetime is extremely long (hours).

https://dx.doi.org/10.1021/acs.cgd.0c01219
Cryst. Growth Des. 2020, 20, 7951−7962

Under our experimental conditions, we can demonstrate that no nucleation occurs inside the macroscopic DLP after LLPS. We also note that protein crystallization pathways depend strongly on the specific systems and the respective conditions. This work provides evidence of a scenario where an MIP forms, but does not initiate interior nucleation. This scenario is not described in Figure 1a.

Furthermore, we note that the crystallization behavior discussed here (Figure 9) is very similar to the "Bergeron process", i.e., crystal growth via vapor deposition at the expense of the metastable DLP. The Bergeron process has been used to describe the water condensation process at high altitudes and the fluid−solid phase transition in colloidal systems.[74] Once crystals are formed, crystal growth via vapor deposition (here: from the dilute phase) is more favored than growth through the supercooled water droplets (here: DLP) due to different saturation vapor pressures of the crystals and the metastable droplets. We can easily compare these two cases because of the existence of a metastable LLPS, resulting in a gas (dilute) and a liquid (dense) phase. This can also explain why crystals are observed to grow into the dilute phase instead of into the dense phase after nucleation.

Crystal Structure of HSA−Y^{3+} Crystals by Single Crystal X-ray Diffraction and the Role of Multivalent Metal Ions. Optimizing crystallization conditions of HSA with YCl_3 leads to high-quality crystals, the structure of which is presented in the following. Before we introduce the crystal structure analysis, we first compare the overall crystal structure of crystals grown with different salts under various conditions. Crystals grown under different conditions and with different morphologies were collected and filled into quartz capillaries for SAXS measurements. As shown in Figure 10, the SAXS profiles of all crystals have Bragg peaks at very similar positions and with similar intensities. The corresponding Miller indices for the first Bragg peaks are also shown. From this agreement, it can be concluded that the crystals of different shape and of different salts have a similar crystal structure. This result is in good agreement with the fact that yttrium and cerium are chemically similar to each other[31] and the phase behavior of HSA solutions in the presence of the two cations is also similar. Nevertheless, for growing high-quality single crystals suitable for X-ray diffraction, HSA with YCl_3 turned out to be the more reliable system. Hence, the crystal structure analysis is performed with HSA−YCl_3 crystals.

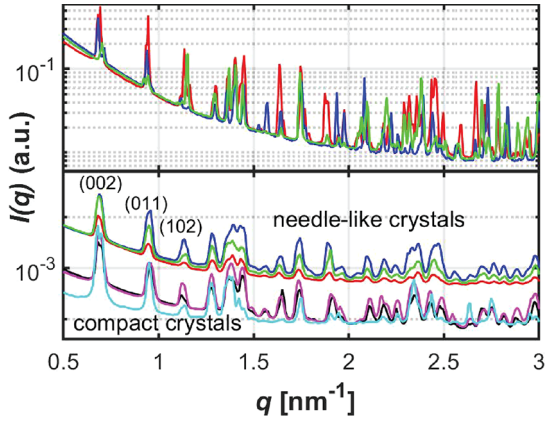

Figure 10. Comparison of SAXS profiles of HSA crystals grown under different conditions with different morphologies and different salts measured at different positions in the capillary. Top: 150 mg/mL HSA with 10 mM $CeCl_3$. Bottom: 30 mg/mL HSA with 3 mM YCl_3 resulting in different morphologies, which are shifted for clarity. The Bragg peaks can be assigned to the corresponding Miller indices using the HSA crystal structure determined in this article (PDB code: 7A9C).

Yttrium causes HSA to crystallize in a so-far not-described crystal form with spacegroup $P2_12_12_1$ and unit cell dimensions of a = 55.27 Å, b = 71.93 Å, c = 180.13 Å, respectively. Nonetheless, the overall fold of the protein is not influenced by the metal ions and is virtually identical with the HSA structures deposited in the PDB database possessing a Cα-rms deviation of 0.84 Å for 579 out of 581 aligned amino acids. The model quality is reasonable for the given resolution of 2.75 Å and is allowed to clearly identify the yttrium ions on the basis of an anomalous difference map (coefficient: $|F^+-F^-|$) in combination with the chemical environment.[75] Two chemically different metal ions were identified that interconnect the HSA protomers in the crystal (Figure 11 b and c), resulting in an overall stoichiometry of HSA to Y^{3+} of 1:2. Each HSA protomer is in contact with ten symmetry-related HSA molecules, but only four protomers out of these are mediated by yttrium interactions. The coordination of the yttrium ions is comparable to the interactions observed for BLG (PDB code: 3PH5, 3PH6) and shows that each yttrium ion is coordinated by three negatively charged glutamate side chains, thereby compensating the positive charge of the metal ion.

We performed an interface calculation, i.e., the ratio between the surface of the binding sites and the total surface of the protein, using PISA[76] to analyze the metal ion contribution for the crystallization of HSA and BLG (PDB code: 3PH5) in the presence of yttrium. The total interface area in the HSA:Y^{3+} crystals is calculated to be 2052 Å^2 out of which 316 Å^2 (15.4%) is mediated by Y^{3+}−protein interactions. This is in good agreement with the observation that most of the contacts of the 585 amino acid long protomers are formed by protein−protein interactions and the influence of the metal ion is less pronounced for HSA. This is different for BLG−Y^{3+} crystals where the yttrium ions contribute more substantially to the crystal contact formation. Here, the four yttrium ions of the dimeric protein make up 30.2% of the total crystal contact area (577 Å^2 out of 1907 Å^2).

In summary, we show that the high valency metal ions bridge the proteins and develop two new protein contacts, which stabilize the crystal lattice for both metal salts used. This is in contrast to the crystal structure of BLG in the presence of YCl_3 where all four binding sites contribute to the bridging contacts between the unit cell.[28] In addition to their crucial role in inducing crystallization, the trivalent cations can be used to solve the phase problem using anomalous dispersion methods, since they are an integral part of the crystal lattice. Both yttrium ions are coordinated by three glutamate side chains. In addition, a carbonyl coordination of the peptide backbone is found for one yttrium ion (Figure 11b). A stable crystal lattice is formed due to the cation-based contacts interconnecting the proteins. This bridging effect has resulted in the development of an ion-activated patchy colloidal model, which describes theoretically the phase behavior observed experimentally.[39] The significant improvement of both crystal yield and quality using multivalent metal ions and the physical mechanisms revealed in our study provide not only a practical guide for protein crystallization but also an efficient way to tune the effective interactions, phase behavior, and even the exact nucleation pathways of protein crystallization. Further-

https://dx.doi.org/10.1021/acs.cgd.0c01219
Cryst. Growth Des. 2020, 20, 7951−7962

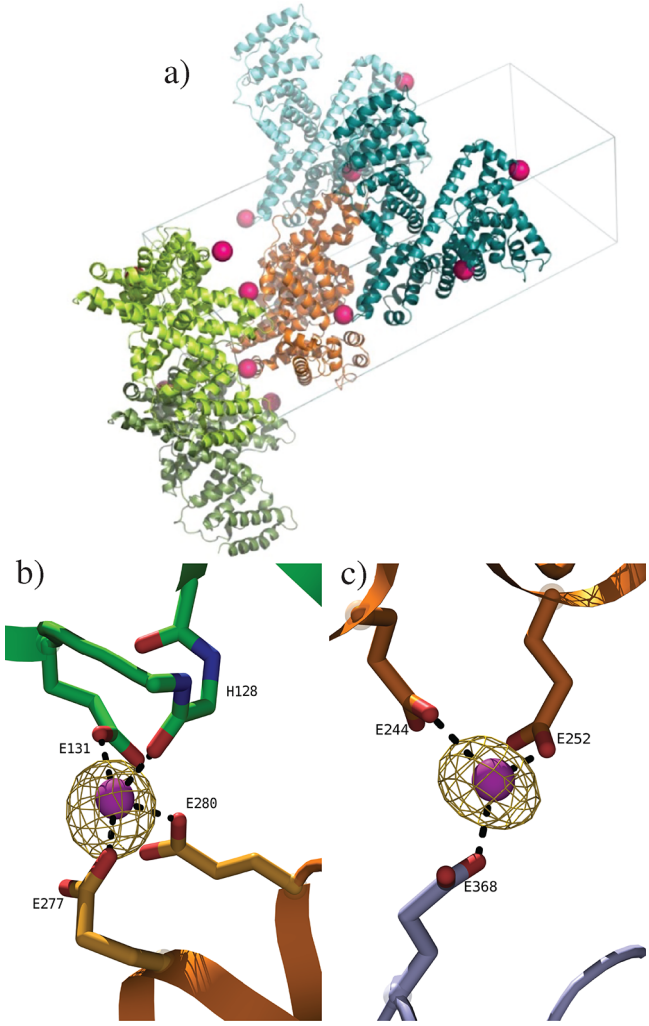

Figure 11. Crystal structure of HSA crystallized in the presence of yttrium ions. The crystal packing is shown for a single protomer. All protomers that contact the central protomer (orange) by metal (pink) coordination are colored (green, blue). All attached protomers interacting exclusively by protein−protein interactions are not visualized. A similar figure showing all crystal contacts of a single protomer can be found in Figure S5. Four of the 10 protomers contact the central protomer by two chemically different metal sites (hot pink) (b, c). The metal sites were placed on the basis of an anomalous electron density map (yellow, contour level 6.0) using the Bijvoet pairs as map coefficients.

more, the ion-activated patchy particle model[39] provides a theoretical framework for future developments in this field.

CONCLUSION

In summary, we have studied protein crystallization in solutions exhibiting a metastable LLPS. We focus on the effects of unstable and metastable DLPs on the crystallization pathways of HSA. Based on the phase diagram, for the first condition outside the LLPS region, but still inside the condensed regime, the DLP is unstable with respect to crystallization and the solution. However, the surface of the quartz cuvette containing the sample may lead to a wetting layer of surface-enhanced dense phase. The second condition is located inside the LLPS binodal, leading to a small amount of metastable DLP. Optical microscopy and SAXS/SANS measurements solely show a monotonous crystal growth. We note that no evidence of nucleation inside the DLPs has been found. Thus, the existence of a metastable LLPS does not seem to be a sufficient condition for two-step nucleation. In our systems, the crystallization process can be better described as a Bergeron process, i.e., crystal growth via vapor deposition (here: from the dilute phase) at the expense of the metastable (or unstable) phase (see Figure 9). The Bergeron process also explains the fact that experimental observations often reveal that the crystals grow inside the dilute phase instead of the dense phase. Furthermore, all crystals grown under different conditions and with different trivalent salts share the same crystal structure. Crystallographic analysis shows that two metal ions are coordinated by negatively charged acidic residues to form intermolecular crystal contacts, hence contributing to the formation of the crystal lattice and supporting the ion-activated patchy particle model.[39]

ASSOCIATED CONTENT

Supporting Information

The Supporting Information is available free of charge at https://pubs.acs.org/doi/10.1021/acs.cgd.0c01219.

Video of the crystallization process recorded by the microscope (MP4)

Additional optical microscopy images, SANS data and the corresponding analysis, fit parameters, crystal structure data collection and refinement statistics, and the crystal structure including protein−protein contacts (PDF)

AUTHOR INFORMATION

Corresponding Authors

Fajun Zhang − *Institut für Angewandte Physik, Universität Tübingen, 72076 Tübingen, Germany;* orcid.org/0000-0001-7639-8594; Email: fajun.zhang@uni-tuebingen.de

Thilo Stehle − *Interfakultäres Institut für Biochemie, Universität Tübingen, 72076 Tübingen, Germany; Department of Pediatrics, Vanderbilt University School of Medicine, Nashville, Tennessee 37232, United States;* orcid.org/0000-0002-4571-8548; Email: thilo.stehle@uni-tuebingen.de

Authors

Ralph Maier − *Institut für Angewandte Physik, Universität Tübingen, 72076 Tübingen, Germany;* orcid.org/0000-0003-3428-039X

Georg Zocher − *Interfakultäres Institut für Biochemie, Universität Tübingen, 72076 Tübingen, Germany*

Andrea Sauter − *Institut für Angewandte Physik, Universität Tübingen, 72076 Tübingen, Germany*

Stefano Da Vela − *Institut für Angewandte Physik, Universität Tübingen, 72076 Tübingen, Germany;* orcid.org/0000-0002-1700-4759

Olga Matsarskaia − *Institut für Angewandte Physik, Universität Tübingen, 72076 Tübingen, Germany;* orcid.org/0000-0002-7293-7287

Ralf Schweins − *Institut Laue-Langevin, 38000 Grenoble, France;* orcid.org/0000-0001-8078-2089

Michael Sztucki − *European Synchrotron Radiation Facility, 38000 Grenoble, France;* orcid.org/0000-0002-5314-9402

https://dx.doi.org/10.1021/acs.cgd.0c01219
Cryst. Growth Des. 2020, 20, 7951−7962

Frank Schreiber − *Institut für Angewandte Physik, Universität Tübingen, 72076 Tübingen, Germany;* orcid.org/0000-0003-3659-6718

Complete contact information is available at: https://pubs.acs.org/10.1021/acs.cgd.0c01219

Notes

The authors declare no competing financial interest.
Present Address for O.M.: Institut Laue-Langevin, 71 avenue des Martyrs, 38000 Grenoble, France.

■ ACKNOWLEDGMENTS

We thank Melanie Oelker, Melanie Eckert, and Marcus Mikorski for experimental assistance and discussions. We gratefully acknowledge the allocation of beamtime at the SLS, the ESRF and the ILL. O.M. acknowledges a fellowship by the Studienstiftung des Deutschen Volkes. F.Z. expresses thanks for the support from the Open Research Fund of the State Key Laboratory of Polymer Physics and Chemistry, Changchun Institute of Applied Chemistry, Chinese Academy of Sciences. The authors thank the DFG for financial support.

■ REFERENCES

(1) Gibbs, J. W. On the equilibrium of heterogeneous substances. *Trans. Connect. Acad. Sci.* **1876**, *16*, 343−524.
(2) Gibbs, J. W. On the equilibrium of heterogeneous substances. *Trans. Connect. Acad. Sci.* **1878**, *3*, 108−248.
(3) Volmer, M.; Weber, A. Keimbildung in übersättigten Gebilden. *Z. Phys. Chem.* **1926**, *119U*, 277−301.
(4) Schubert, R.; Meyer, A.; Baitan, D.; Dierks, K.; Perbandt, M.; Betzel, C. Real-Time Observation of Protein Dense Liquid Cluster Evolution during Nucleation in Protein Crystallization. *Cryst. Growth Des.* **2017**, *17*, 954−958.
(5) Zhang, F. Nonclassical nucleation pathways in protein crystallization. *J. Phys.: Condens. Matter* **2017**, *29*, 443002.
(6) Meldrum, F. C.; Sear, R. P. Now You See Them. *Science* **2008**, *322*, 1802−1803.
(7) Erdemir, D.; Lee, A. Y.; Myerson, A. S. Nucleation of Crystals from Solution: Classical and Two-Step Models. *Acc. Chem. Res.* **2009**, *42*, 621−629.
(8) Sear, R. P. The non-classical nucleation of crystals: microscopic mechanisms and applications to molecular crystals, ice and calcium carbonate. *Int. Mater. Rev.* **2012**, *57*, 328−356.
(9) Russo, J.; Tanaka, H. Crystal nucleation as the ordering of multiple order parameters. *J. Chem. Phys.* **2016**, *145*, 211801.
(10) Karthika, S.; Radhakrishnan, T. K.; Kalaichelvi, P. A Review of Classical and Nonclassical Nucleation Theories. *Cryst. Growth Des.* **2016**, *16*, 6663−6681.
(11) Van Driessche, A. E.; Van Gerven, N.; Bomans, P. H.; Joosten, R. R.; Friedrich, H.; Gil-Carton, D.; Sommerdijk, N. A.; Sleutel, M. Molecular nucleation mechanisms and control strategies for crystal polymorph selection. *Nature* **2018**, *556*, 89.
(12) ten Wolde, P. R.; Frenkel, D. Enhancement of Protein Crystal Nucleation by Critical Density Fluctuations. *Science* **1997**, *277*, 1975−1978.
(13) Vekilov, P. G. Dense Liquid Precursor for the Nucleation of Ordered Solid Phases from Solution. *Cryst. Growth Des.* **2004**, *4*, 671−685.
(14) Sleutel, M.; van Driessche, A. E. S. Role of clusters in nonclassical nucleation and growth of protein crystals. *Proc. Natl. Acad. Sci. U. S. A.* **2014**, *111*, E546−E553.
(15) Russo, J.; Tanaka, H. The microscopic pathway to crystallization in supercooled liquids. *Sci. Rep.* **2012**, *2*, 505.
(16) Hagen, M. H. J.; Frenkel, D. Determination of phase diagrams for the hard-core attractive Yukawa system. *J. Chem. Phys.* **1994**, *101*, 4093−4097.
(17) Cardinaux, F.; Gibaud, T.; Stradner, A.; Schurtenberger, P. Interplay between Spinodal Decomposition and Glass Formation in Proteins Exhibiting Short-Range Attractions. *Phys. Rev. Lett.* **2007**, *99*, 118301.
(18) Da Vela, S.; Exner, C.; Schäufele, R. S.; Möller, J.; Fu, Z.; Zhang, F.; Schreiber, F. Arrested and temporarily arrested states in a protein-polymer mixture studied by USAXS and VSANS. *Soft Matter* **2017**, *13*, 8756−8765.
(19) Begam, N.; Matsarskaia, O.; Sztucki, M.; Zhang, F.; Schreiber, F. Unification of lower and upper critical solution temperature phase behavior of globular protein solutions in the presence of multivalent cations. *Soft Matter* **2020**, *16*, 2128−2134.
(20) Gripon, C.; Legrand, L.; Rosenman, I.; Vidal, O.; Robert, M. C.; Boué, F. Lysozyme Solubility in H_2O and D_2O Solutions: A Simple Relationship. *J. Cryst. Growth* **1997**, *177*, 238−247.
(21) Gripon, C.; Legrand, L.; Rosenman, I.; Vidal, O.; Robert, M. C.; Boué, F. Lysozyme-lysozyme interactions in under- and supersaturated solutions: a simple relation between the second virial coefficients in H_2O and D_2O. *J. Cryst. Growth* **1997**, *178*, 575−584.
(22) Bucciarelli, S.; Mahmoudi, N.; Casal-Dujat, L.; Jéhannin, M.; Jud, C.; Stradner, A. Extended law of corresponding states applied to solvent isotope effect on a globular protein. *J. Phys. Chem. Lett.* **2016**, *7*, 1610−1615.
(23) Braun, M. K.; Wolf, M.; Matsarskaia, O.; Da Vela, S.; Roosen-Runge, F.; Sztucki, M.; Roth, R.; Zhang, F.; Schreiber, F. Strong Isotope Effects on Effective Interactions and Phase Behavior in Protein Solutions in the Presence of Multivalent Ions. *J. Phys. Chem. B* **2017**, *121*, 1731−1739.
(24) Vekilov, P. G. Nucleation. *Cryst. Growth Des.* **2010**, *10*, 5007−5019.
(25) Sauter, A.; Oelker, M.; Zocher, G.; Zhang, F.; Stehle, T.; Schreiber, F. Nonclassical Pathways of Protein Crystallization in the Presence of Multivalent Metal Ions. *Cryst. Growth Des.* **2014**, *14*, 6357−6366.
(26) Sauter, A.; Roosen-Runge, F.; Zhang, F.; Lotze, G.; Jacobs, R. M. J.; Schreiber, F. Real-Time Observation of Nonclassical Protein Crystallization Kinetics. *J. Am. Chem. Soc.* **2015**, *137*, 1485−1491.
(27) Sauter, A.; Roosen-Runge, F.; Zhang, F.; Lotze, G.; Feoktystov, A.; Jacobs, R. M. J.; Schreiber, F. On the question of two-step nucleation in protein crystallization. *Faraday Discuss.* **2015**, *179*, 41−58.
(28) Zhang, F.; Zocher, G.; Sauter, A.; Stehle, T.; Schreiber, F. Novel approach to controlled protein crystallization through ligandation of yttrium cations. *J. Appl. Crystallogr.* **2011**, *44*, 755−762.
(29) Zhang, F.; Roosen-Runge, F.; Sauter, A.; Wolf, M.; Jacobs, R. M. J.; Schreiber, F. Reentrant Condensation, Liquid-Liquid Phase Separation and Crystallization in Protein Solutions Induced by Multivalent Metal Ions. *Pure Appl. Chem.* **2014**, *86*, 191−202.
(30) Djinović-Carugo, K.; Carugo, O. Structural biology of the lanthanides - Mining rare earths in the Protein Data Bank. *J. Inorg. Biochem.* **2015**, *143*, 69.
(31) Daumann, L. J. Essential and Ubiquitous: The Emergence of Lanthanide Metallobiochemistry. *Angew. Chem., Int. Ed.* **2019**, *58*, 12795−12802.
(32) Matsarskaia, O.; Roosen-Runge, F.; Schreiber, F. Multivalent ions and biomolecules: Attempting a comprehensive perspective. *ChemPhysChem* **2020**, *21*, 1742−1767.
(33) Deng, Y. W.; Ro, S. Y.; Rosenzweig, A. C. Structure and function of the lanthanide-dependent methanol dehydrogenase XoxF from the methanotroph Methylomicrobium buryatense 5GB1C. *JBIC, J. Biol. Inorg. Chem.* **2018**, *23*, 1037−1047.
(34) Nguyen, T. T.; Rouzina, I.; Shklovskii, B. I. Reentrant condensation of DNA induced by multivalent counterions. *J. Chem. Phys.* **2000**, *112*, 2562−2568.
(35) Matsarskaia, O.; Roosen-Runge, F.; Lotze, G.; Möller, J.; Mariani, A.; Zhang, F.; Schreiber, F. Tuning phase transitions of aqueous protein solutions by multivalent cations. *Phys. Chem. Chem. Phys.* **2018**, *20*, 27214−27225.

(36) Zhang, F.; Weggler, S.; Ziller, M. J.; Ianeselli, L.; Heck, B. S.; Hildebrandt, A.; Kohlbacher, O.; Skoda, M. W. A.; Jacobs, R. M. J.; Schreiber, F. Universality of protein reentrant condensation in solution induced by multivalent metal ions. *Proteins: Struct., Funct., Genet.* **2010**, *78*, 3450−3457.
(37) Zhang, F.; Roth, R.; Wolf, M.; Roosen-Runge, F.; Skoda, M. W. A.; Jacobs, R. M. J.; Stzucki, M.; Schreiber, F. Charge-controlled metastable liquid-liquid phase separation in protein solutions as a universal pathway towards crystallization. *Soft Matter* **2012**, *8*, 1313−1316.
(38) Pandit, S.; Kundu, S. Optical responses of BSA protein under re-entrant condensation in presence of trivalent ions. *J. Mol. Liq.* **2019**, *276*, 954−960.
(39) Roosen-Runge, F.; Zhang, F.; Schreiber, F.; Roth, R. Ion-activated Attractive Patches as a Mechanism for Controlled Protein Interactions. *Sci. Rep.* **2015**, *4*, 7016.
(40) Bijelic, A.; Rompel, A. The use of polyoxometalates in protein crystallography − An attempt to widen a well-known bottleneck. *Coord. Chem. Rev.* **2015**, *299*, 22−38.
(41) Zhang, F.; Skoda, M. W. A.; Jacobs, R. M. J.; Zorn, S.; Martin, R. A.; Martin, C. M.; Clark, G. F.; Weggler, S.; Hildebrandt, A.; Kohlbacher, O.; Schreiber, F. Reentrant Condensation of Proteins in Solution Induced by Multivalent Counterions. *Phys. Rev. Lett.* **2008**, *101*, 148101.
(42) Wolf, M.; Roosen-Runge, F.; Zhang, F.; Roth, R.; Skoda, M. W.; Jacobs, R. M.; Sztucki, M.; Schreiber, F. Effective interactions in protein−salt solutions approaching liquid−liquid phase separation. *J. Mol. Liq.* **2014**, *200*, 20−27.
(43) Zhang, F.; Roosen-Runge, F.; Sauter, A.; Roth, R.; Skoda, M. W. A.; Jacobs, R.; Sztucki, M.; Schreiber, F. The Role of Cluster Formation and Metastable Liquid-Liquid Phase Separation in Protein Crystallization. *Faraday Discuss.* **2012**, *159*, 313−325.
(44) Muschol, M.; Rosenberger, F. Liquid−liquid phase separation in supersaturated lysozyme solutions and associated precipitate formation/crystallization. *J. Chem. Phys.* **1997**, *107*, 1953−1962.
(45) Chen, Q.; Vekilov, P. G.; Nagel, R. L.; Hirsch, R. E. Liquid-Liquid Phase Separation in Hemoglobins: Distinct Aggregation Mechanisms of the β6 Mutants. *Biophys. J.* **2004**, *86*, 1702−1712.
(46) Ray, W. J.; Bracker, C. Polyethylene glycol: catalytic effect on the crystallization of phosphoglucomutase at high salt concentration. *J. Cryst. Growth* **1986**, *76*, 562−576.
(47) Liu, Y.; Wang, X.; Ching, C. B. Toward Further Understanding of Lysozyme Crystallization: Phase Diagram, Protein-Protein Interaction, Nucleation Kinetics, and Growth Kinetics. *Cryst. Growth Des.* **2010**, *10*, 548−558.
(48) Sober, H. A. *CRC Handbook of Biochemistry: Selected data for molecular biology*; The Chemical Rubber Co.: Cleveland, OH, 1970.
(49) Narayanan, T.; Sztucki, M.; Van Vaerenbergh, P.; Léonardon, J.; Gorini, J.; Claustre, L.; Sever, F.; Morse, J.; Boesecke, P. A multipurpose instrument for time-resolved ultra-small-angle and coherent X-ray scattering. *J. Appl. Crystallogr.* **2018**, *51*, 1511−1524.
(50) Narayanan, T. Synchroton small-angle X-ray Scattering. In *Soft Matter Characterization*; Borsali, R., Pecora, R., Eds.; Springer New York, 2008; Chapter 17.
(51) Ianeselli, L.; Zhang, F.; Skoda, M. W. A.; Jacobs, R. M. J.; Martin, R. A.; Callow, S.; Prévost, S.; Schreiber, F. Protein-protein interactions in ovalbumin solutions studied by small-angle scattering: effect of ionic strength and the chemical nature of cations. *J. Phys. Chem. B* **2010**, *114*, 3776−3783.
(52) Lieutenant, K.; Lindner, P.; Gahler, R. A new design for the standard pinhole small-angle neutron scattering instrument D11. *J. Appl. Crystallogr.* **2007**, *40*, 1056−1063.
(53) Könnecke, M.; Akeroyd, F. A.; Bernstein, H. J.; Brewster, A. S.; Campbell, S. I.; Clausen, B.; Cottrell, S.; Hoffmann, J. U.; Jemian, P. R.; Männicke, D.; et al. The NeXus data format. *J. Appl. Crystallogr.* **2015**, *48*, 301−305.
(54) Richard, D.; Ferrand, M.; Kearley, G. J. Analysis and visualisation of neutron-scattering data. *J. Neutron Res.* **1996**, *4*, 33−39.
(55) Zhang, F.; Beck, C.; Braun, M.; Da Vela, S.; Maier, R.; Matsarskaia, O.; Mikorski, M.; Roosen-Runge, F.; Schreiber, F.; Schweins, R.; Seydel, T.; Sohmen, B. *Kinetics of two-step nucleation in protein crystallization studied by real-time SANS*; Institut Laue-Langevin (ILL): 2016; DOI: 10.5291/ILL-DATA.9-13-672.
(56) Kabsch, W. XDS. *Acta Crystallogr., Sect. D: Biol. Crystallogr.* **2010**, *66*, 125−132.
(57) McCoy, A. J.; Grosse-Kunstleve, R. W.; Adams, P. D.; Winn, M. D.; Storoni, L. C.; Read, R. J. Phaser crystallographic software. *J. Appl. Crystallogr.* **2007**, *40*, 658−674.
(58) Afonine, P. V.; Grosse-Kunstleve, R. W.; Echols, N.; Headd, J. J.; Moriarty, N. W.; Mustyakimov, M.; Terwilliger, T. C.; Urzhumtsev, A.; Zwart, P. H.; Adams, P. D. Towards automated crystallographic structure refinement with *phenix.refine*. *Acta Crystallogr., Sect. D: Biol. Crystallogr.* **2012**, *68*, 352−367.
(59) Murshudov, G. N.; Skubák, P.; Lebedev, A. A.; Pannu, N. S.; Steiner, R. A.; Nicholls, R. A.; Winn, M. D.; Long, F.; Vagin, A. A. *REFMAC5* for the refinement of macromolecular crystal structures. *Acta Crystallogr., Sect. D: Biol. Crystallogr.* **2011**, *67*, 355−367.
(60) Emsley, P.; Lohkamp, B.; Scott, W. G.; Cowtan, K. Features and development of Coot. *Acta Crystallogr., Sect. D: Biol. Crystallogr.* **2010**, *66*, 486−501.
(61) Chen, V. B.; Arendall, W. B., III; Headd, J. J.; Keedy, D. A.; Immormino, R. M.; Kapral, G. J.; Murray, L. W.; Richardson, J. S.; Richardson, D. C. *MolProbity*: all-atom structure validation for macromolecular crystallography. *Acta Crystallogr., Sect. D: Biol. Crystallogr.* **2010**, *66*, 12−21.
(62) Schrödinger, L. *PyMOL Molecular Graphics System*, Version 1.8; Schrödinger, LLC.: 2015.
(63) Braun, M. K.; Sauter, A.; Matsarskaia, O.; Wolf, M.; Roosen-Runge, F.; Sztucki, M.; Roth, R.; Zhang, F.; Schreiber, F. Reentrant Phase Behavior in Protein Solutions Induced by Multivalent Salts: Strong Effect of Anions Cl−Versus NO3−. *J. Phys. Chem. B* **2018**, *122*, 11978−11985.
(64) Fries, M. R.; Stopper, D.; Braun, M. K.; Hinderhofer, A.; Zhang, F.; Jacobs, R. M.; Skoda, M. W.; Hansen-Goos, H.; Roth, R.; Schreiber, F. Multivalent-ion-activated protein adsorption reflecting bulk reentrant behavior. *Phys. Rev. Lett.* **2017**, *119*, 228001.
(65) Fries, M. R.; Stopper, D.; Skoda, M. W. A.; Blum, M.; Kertzscher, C.; Hinderhofer, A.; Zhang, F.; Jacobs, R. M. J.; Roth, R.; Schreiber, F. Enhanced protein adsorption upon bulk phase separation. *Sci. Rep.* **2020**, *10*, 10349.
(66) De Gennes, P.-G. Wetting: statics and dynamics. *Rev. Mod. Phys.* **1985**, *57*, 827.
(67) Vliegenthart, G. A.; Lekkerkerker, H. N. W. Predicting the gas−liquid critical point from the second virial coefficient. *J. Chem. Phys.* **2000**, *112*, 5364−5369.
(68) Verhulst, P.-F. Notice sur la loi que la population suit dans son accroissement. *Corresp. Math. Phys.* **1838**, *10*, 113−126.
(69) Kritsman, V. A. Ludwig Wilhelmy, Jacobus H. van't Hoff, Svante Arrhenius und die Geschichte der chemischen Kinetik. *Chem. Unserer Zeit* **1997**, *31*, 291−300.
(70) Kuznetsov, Y.; Malkin, A.; McPherson, A. Atomic-force-microscopy studies of phase separations in macromolecular systems. *Phys. Rev. B: Condens. Matter Mater. Phys.* **1998**, *58*, 6097−6103.
(71) Vivarès, D.; Kaler, E. W.; Lenhoff, A. M. Quantitative imaging by confocal scanning fluorescence microscopy of protein crystallization *via* liquid−liquid phase separation. *Acta Crystallogr., Sect. D: Biol. Crystallogr.* **2005**, *61*, 819−825.
(72) Galkin, O.; Vekilov, P. G. Are Nucleation Kinetics of Protein Crystals Similar to Those of Liquid Droplets? *J. Am. Chem. Soc.* **2000**, *122*, 156−163.
(73) Yamazaki, T.; Kimura, Y.; Vekilov, P. G.; Furukawa, E.; Shirai, M.; Matsumoto, H.; Van Driessche, A. E. S.; Tsukamoto, K. Two types of amorphous protein particles facilitate crystal nucleation. *Proc. Natl. Acad. Sci. U. S. A.* **2017**, *114*, 2154−2159.
(74) Tsurusawa, H.; Russo, J.; Leocmach, M.; Tanaka, H. Formation of porous crystals via viscoelastic phase separation. *Nat. Mater.* **2017**, *16*, 1022−1028.

https://dx.doi.org/10.1021/acs.cgd.0c01219
Cryst. Growth Des. 2020, 20, 7951−7962

(75) Mueller-Dieckmann, C.; Panjikar, S.; Schmidt, A.; Mueller, S.; Kuper, J.; Geerlof, A.; Wilmanns, M.; Singh, R. K.; Tucker, P. A.; Weiss, M. S. On the routine use of soft X-rays in macromolecular crystallography. Part IV. Efficient determination of anomalous substructures in biomacromolecules using longer X-ray wavelengths. *Acta Crystallogr., Sect. D: Biol. Crystallogr.* **2007**, *63*, 366−380.
(76) Krissinel, E.; Henrick, K. Inference of macromolecular assemblies from crystalline state. *J. Mol. Biol.* **2007**, *372*, 774−797.

https://dx.doi.org/10.1021/acs.cgd.0c01219
Cryst. Growth Des. 2020, 20, 7951−7962